Boundary-Layer Meteorology (2025) 191:17
https://doi.org/10.1007/s10546-025-00908-x

RESEARCH ARTICLE

$\mathscr{L}$-moments Reveal the Scales of Momentum Transport in Dense Canopy Flows

Subharthi Chowdhuri[1] · **Olli Peltola**[1]

Received: 13 September 2024 / Accepted: 19 February 2025 / Published online: 14 March 2025
© The Author(s) 2025

Abstract
The interaction between a dense forest canopy and atmosphere is a complex fluid-dynamical problem with a wide range of practical applications, spanning from the aspects of carbon sequestration to the spread of wildfires through a forest. To delineate the eddy processes specific to canopy flows, we develop an $\mathscr{L}$-moment based event framework and apply it on a suite of observational datasets encompassing both canopy and atmospheric surface layer flows. In this framework, the turbulent fluctuations are considered as a chronicle of positive and negative events having finite lengths or time scales, whose statistical distributions are quantified through the $\mathscr{L}$ moments. $\mathscr{L}$ moments are statistically more robust than the conventional moments and have earlier been used in hydrology applications, but here we show how this concept is useful to identify the contrasting features between canopy and atmospheric surface layer flows. The $\mathscr{L}$-moment framework is complemented with wavelet analysis, revealing how differently the canopy-scale coherent structures modulate the horizontal and vertical velocity components in sub-canopy environments. We hypothesize that a consequence of this phenomenon is the existence of two different eddy processes with distinct scaling properties that transport momentum in the gradient and counter-gradient directions, respectively. These findings shed light on a long-standing issue in canopy flows: why the integral timescale of vertical velocity increases as the heights approach the forest floor?

Keywords Canopy flows · Event framework · $\mathscr{L}$-moment · Momentum transport · Wavelet analysis

1 Introduction

Forests cover nearly 30% of the Earth's surface and they regulate the Earth's surface temperature, emit bio-aerosol particles that act as cloud condensation nuclei, and sequester carbon from the atmosphere, thereby playing the role of a carbon sink. From a micrometeorological perspective, how the trees in a dense forest interact with the lowest layers of the atmosphere where the air is turbulent, remains a complex fluid-dynamical problem and therefore is a subject of great scrutiny (Raupach and Thom 1981; Finnigan 2000; Brunet 2020). Despite the complexities, this problem is important since to improve the parameterization of land-atmosphere exchanges in weather and climate models, the characteristics of turbulent

✉ Subharthi Chowdhuri
subharthi.chowdhuri@luke.fi

[1] Natural Resources Institute Finland (Luke), Latokartanonkaari 9, 00790 Helsinki, Finland

transport in vegetation canopies need to be better represented (Harman and Finnigan 2007; Bonan et al. 2018). A part of this complexity arises because, unlike the atmospheric surface layer flow, the vertically distributed drag associated with the presence of a vegetation canopy and its foliage, introduces additional length scales that modulate the turbulence structure inside the canopy.

In particular, the seminal study by Raupach et al. (1996) introduced a mixing layer model and showed that an inflection point in the mean velocity profile at the canopy top induces Kelvin-Helmholtz (KH) instabilities that penetrate the canopy volume, which could be regarded as the canopy-scale coherent structures or the mixing layer eddies. Moreover, the flow within a canopy is obstructed by the presence of individual canopy elements, which, in turn, produce a lot of fine-scale turbulence bearing a strong resemblance with a von Kármán vortex shedding mechanism (Poggi and Katul 2009; Ghannam et al. 2015). Additionally, the attached eddies, whose sizes are proportional to the height above the surface and are commonly found in atmospheric surface layer flows, remain superposed on the canopy-scale motions. Based on this eddy structure, Poggi et al. (2004) proposed a simple three-layer mixing-length type model for canopy flows. In this model, it was assumed that the layers deep within the canopy are only affected by the von Kármán eddies, the middle canopy layer has influences from both canopy scale eddies and attached eddy motions, while the upper layers of the canopy only feel the influence of the attached eddies. As one may realize, an inherent assumption in this formulation is the eddies generated at the canopy top do not exert significant influences at heights deep within the canopy.

On the other hand, the studies by Ghisalberti and Nepf (2002) and Chung and Koseff (2021) on aquatic vegetation canopies and canopies artificially generated in a laboratory, hypothesized that there exists a certain height up to which the mixing layer eddies penetrate within a canopy. Chung and Koseff (2021) defined this height as $h - z_p$, where h is the canopy height and z_p is the vertical distance from the canopy floor to the height where the momentum flux falls to about 10% of the maximum momentum flux at the canopy top. In the case of aquatic canopies, Nepf (2012) posited a length scale δ_e that gave an estimate of the depth to which mixing layer eddies penetrate within a canopy, when the conditions are conducive for the formation of KH instabilities. This δ_e was shown to be dependent on the density of the canopy. However, for terrestrial deciduous canopies, Perret and Patton (2021) found that the eddy motions deep within a canopy (without specifying whether the canopy was dense according to the criterion of Nepf (2012)) were modulated by the canopy-scale coherent structures. A similar finding was reported by Cava et al. (2022), where they demonstrated that the momentum transport events deep within the Amazon forest carried the signatures of the mixing layer eddies. They specifically highlighted the role of counter-gradient momentum transport in that regard. Recently, Peltola et al. (2021) developed a criterion to determine whether the eddy motions occurring across the canopy depth are strongly coupled with the forest floor or not. Their criterion is contingent on how frequently the negative vertical velocity fluctuations (downdrafts) at the canopy top exceed a certain threshold, which, in turn, depends on canopy density and thermal stratification of air. Therefore, it appears that the canopy scale coherent structures or mixing layer eddies can extend their footprints deep down the canopy, although they might not actively participate in the transport of momentum.

Regarding momentum transport in canopy flows, the earlier studies found a difference between the ejection and sweep motions for heights within and above a canopy (Thomas and Foken 2007; Brunet 2020). In line with the quadrant nomenclature, these ejection and sweep motions were identified as the conditions when $u < 0$, $w > 0$ and $u > 0$, $w < 0$, respectively, where u and w are the turbulent fluctuations in the streamwise and vertical directions. These studies showed that the contributions to the momentum flux within the canopies were mostly

dominated by sweeps, while above the canopies ejections played a more significant role. However, a traditional quadrant analysis does not provide any information about the time scales of these different quadrant motions. To fill that gap, Chowdhuri et al. (2022) conducted a persistence analysis on the momentum flux events for a dense canopy flow. They considered the time scales of the four quadrants separately by simply estimating how much time they spend in a particular quadrant state before switching to an another one. By doing so, they plotted the probability density functions (PDFs) of these time scales for the four quadrants that included the counter-gradient ones for which the momentum fluxes were positive. They found that the time scale PDFs of the ejection and sweep events remained remarkably invariant with height and displayed no changes within or above the canopy. On the contrary, the time scale PDFs of the counter-gradient events were quite sensitive to the location. For instance, these PDFs showed heavy tails within the canopy but those progressively disappeared as the heights approached the canopy top.

These height variations in the PDFs of counter-gradient time scales were also reflected in the persistence PDFs of vertical velocity fluctuations. In this case, the time scales were defined as the times the w signal spends either in a positive or in a negative state. Chowdhuri et al. (2022) found that the persistence PDFs of w signals showed a clear bulge for heights within the canopy, meaning more large-scale events populated the vertical velocity fluctuations. Therefore, the w signals appeared to behave more coherently within the canopy than at the heights above it. Some previous studies had reported that the integral time scales of w (γ_w) were larger within the canopy air space as compared to above, although no satisfactory explanation was provided regarding the same (Launiainen et al. 2007; Chamecki 2013). In fact, from large eddy simulations, Patton et al. (2016) observed that the integral length scales of vertical velocity diminished at heights above the canopy. In field-experimental datasets, this behavior is not documented well since a more standard practice to plot the vertical profiles of γ_w is by multiplying them with the local mean wind speed (Taylor's hypothesis), whose values itself decrease significantly within the canopy (Finnigan 2000). As a result, the integral length scales of vertical velocity appear small within the canopy sub layers. It is worth noting that the applicability of Taylor's hypothesis in canopy flows is questionable (Everard et al. 2021).

Despite such interesting observations, the results of Chowdhuri et al. (2022) were qualitative in nature since the persistence PDFs were empirically determined and therefore their properties were not quantified. Due to this limitation, it was not clear what type of eddy processes give rise to the large counter-gradient events in canopy sub layers and how exactly they differ from a canonical atmospheric surface layer flow. In general, the persistence PDFs display an extended power-law regime and thus they fall into the category of heavy-tailed distributions. To quantify such heavy-tailed distributions, conventional statistical moments (such as kurtosis) do not work well since their estimates do not converge satisfactorily (Nair et al. 2022). We demonstrate this in Fig. 1 of this manuscript.

As opposed to conventional moments, in this study, we deal with heavy-tailed distributions by introducing $\mathscr{L}$-moment as a statistical concept and show how it can be used in conjunction with wavelet analysis to reveal novel physical insights about canopy turbulence. $\mathscr{L}$-moments are primarily defined as linear combinations of the order statistics, which are based on the cumulative distribution functions of any stochastic signal. Although the concept of $\mathscr{L}$-moment has been used in hydrology before (Vogel and Fennessey 1993), here we use it to elucidate on the physics of canopy flows. By using this framework, we seek to answer the following research questions: (1) Do the mixing layer eddies penetrate only down to a certain height within the canopy or do they reach all the way down to the forest floor? (2) Why does the integral time scale of vertical velocity (γ_w) increase as the heights decrease

within the canopy? (3) How these two phenomena, i.e. the penetration of mixing layer eddies and increase in γ_w, shape the transport of momentum in canopy flows?

We compare our findings between the atmospheric surface layer and canopy flows by using an extensive range of experimental datasets collected from different geographical locations spanning from the tropics to mid-latitudes. For our analysis, we restrict ourselves to near-neutral conditions, i.e. without the effects of buoyancy. The remainder of this study is organized as follows. In Sect. 2 we introduce the experimental datasets and our framework. In Sect. 3, the results are presented and discussed to elucidate on the canopy flow physics. Finally, in Sect. 4, the conclusions and scope for future research are outlined.

2 Dataset and Methodology

2.1 Dataset

To address our research objectives, we employ two different datasets where measurements were carried out within a homogeneous and dense forest canopy. The flow over these forest canopies can be broadly categorized as roughness sublayer flows or RSL flows. By assuming the depth of the atmospheric boundary layer (δ) to be 500 m, the friction Reynolds number (Re) of these flows can be estimated as $Re = (u_*\delta)/\nu \approx 10^7$, where u_* is the friction velocity at the canopy top and ν is the kinematic viscosity of air. One of these datasets is the GoAmazon one, where nine level sonic anemometer measurements were available at a measurement site named Cuieiras Biological Reserve in Manaus, Brazil (3.12° S, 60° W), surrounded by the dense Amazon forest (Fuentes et al. 2016; Ghannam et al. 2018; Chowdhuri et al. 2022). The measurement heights for the GoAmazon dataset are within the range of $z/h = 0.2 - 1.38$, where h is the canopy height, approximately equal to 35 m. The leaf area index (LAI), which is defined as the total one-sided leaf area (half the total foliage area) per unit ground surface area, is estimated to be between 6.1 and 7.3$\mathrm{m^2 m^{-2}}$. For the Amazon forest, the vertical distribution of leaf area density showed a peak at around $z/h = 0.67$, meaning that this forest had a relatively dense overstory (Dias-Junior et al. 2015). This experiment ran continuously between March 2014 and January 2015, collecting data at a 20-Hz sampling frequency. The second dataset is over Loblolly pine canopies in Duke forest (36° N, 78° W), where only one measurement height is available at $z/h = 1.44$. Here, h is 13 m and the sampling frequency is set at 10 Hz (Katul et al. 1997). The LAI for this forest is 3.1 $\mathrm{m^2\ m^{-2}}$. For both of these RSL datasets, the data were divided into 30-min blocks and a double-coordinate rotation was applied to align the x-axis with the direction of the mean wind. Turbulent fluctuations in the wind components (u, v, and w in the streamwise, cross-stream, and vertical directions respectively) were computed after subtracting the mean. Moreover, in our analysis, we restrict ourselves to near-neutral stratification only, satisfying the condition $|(z-d)/L| < 0.5$, where, z is the observation height, d is the displacement height being equal to $2h/3$, and L is the Obukhov length.

Although the condition $|(z-d)/L| \leq 0.5$ to identify the near-neutral runs is not a strict one, similar choice was made by some previous studies (Cava and Katul 2009; Cava et al. 2012). From a statistical perspective, this criterion ensured that we had sufficient number of 30-min runs to ensemble average the results. Note that for the GoAmazon dataset, the condition $|(z-d)/L| \leq 0.5$ was imposed at and above the canopy top ($z/h = 1$, 1.15, and 1.38). Accordingly, the L values were computed from a near-constant flux profile at these three heights. This ultimately resulted in 93 and 214 blocks of 30-min runs for the GoAmazon

and Duke forest datasets, respectively. While reporting the results in Sect. 3, an average over these ensemble of 30-min runs is performed.

To compare the features of canopy flows with canonical atmospheric surface layer flows (ASL flows), three additional datasets were also used. One of these datasets was collected during the Surface Layer Turbulence and Environmental Science Test (SLTEST) experiment, where nine north-facing time-synchronized sonic anemometers were mounted on a 30-m mast, spaced logarithmically over an 18-fold range of heights, from 1.42 to 25.7 m, with the sampling frequency being set at 20 Hz (McNaughton et al. 2007). This experiment was conducted at the Great Salt Lake desert in Utah, USA (40.14° N, 113.5° W), where the surface conditions were aerodynamically smooth with roughness lengths of the order of millimeters. The other two datasets were obtained during an experimental campaign in India. This experiment is known as the Cloud Aerosol Interaction and Precipitation Enhancement Experiment (CAIPEEX), during which two micrometeorological towers of 20-m height were set up over Mahbubnagar (16.75° N, 78° E) and Varanasi (25.32° N, 83° E) regions. On these towers, only at a single measurement height, the high-frequency observations of the three velocity components were sampled at a frequency of 10-Hz (Chowdhuri and Prabha 2019). The site conditions were representative of a typical grassland with roughness lengths of the order of centimeters, an order of magnitude higher than the SLTEST experiment. Henceforth, we refer to these grassland sites as CPX1 and CPX2, respectively. The measurement heights for these experiments were 5 m and 6 m, respectively. Similar to canopy flows, the results reported in Sect. 3 are averaged over an ensemble of near-neutral runs of 30-min duration each. The near-neutral runs are identified as those satisfying the condition $|z/L| < 0.5$, which resulted in 19 and 170 blocks of 30-min runs for the SLTEST and CAIPEEX datasets, respectively. Despite the number of near-neutral runs being less for the SLTEST datasets, the second-order turbulence statistics (u, w spectra and u-w cospectra) were well-converged for both u and w signals. The mean velocity profiles ($\overline{U}$) are compared between the ASL and RSL flows in Fig. S1a of the Supplementary Material. Here, the SLTEST and GoAmazon datasets are used to represent the ASL and RSL flows, respectively. From Fig. S1a it is evident that, as opposed to ASL flows, $\overline{U}$ values of RSL flows significantly decrease at heights within the canopy due to the absorption of momentum by the foliage.

2.2 $\mathscr{L}$-oment Analysis

The conventional statistical moments are defined as,

$$\overline{X^m} = \int_{-\infty}^{+\infty} X^m P(X) dx, \tag{1}$$

where X is a stochastic signal, $P(X)$ is its probability density function (PDF), and m is the moment order (e.g., $m = 2$ represents variance). The sample estimates of such conventional moments, such as kurtosis ($\mathscr{K}(X)$), are computed in standardized format as,

$$\mathscr{K}(X) = \overline{\left(\frac{X - \overline{X}}{\sigma_X}\right)^4}, \tag{2}$$

where $\overline{X}$ is the sample mean and σ_X is the standard deviation. On the other hand, the $\mathscr{L}$ moments are defined with respect to the cumulative distribution functions (CDFs), instead of the PDFs. As shown by Vogel and Fennessey (1993), the first four $\mathscr{L}$ moments are

theoretically defined as,

$$\begin{aligned}\mathscr{L}_1 &= \beta_0\\ \mathscr{L}_2 &= 2\beta_1 - \beta_0\\ \mathscr{L}_3 &= 6\beta_2 - 6\beta_1 + \beta_0\\ \mathscr{L}_4 &= 20\beta_3 - 30\beta_2 + 12\beta_1 - \beta_0,\end{aligned} \tag{3}$$

where $\beta_r = \mathscr{E}[X(F_X)^r]$, with X being a stochastic signal, F_X is the cumulative distribution function of X, and $\mathscr{E}$ is the expected value. For all practical purposes, these four $\mathscr{L}$ moments can be computed from a stochastic sample X of size N as (Wang 1996),

$$\begin{aligned}\mathscr{L}_1 &= \frac{1}{\binom{N}{1}}\sum_{i=1}^{N} X(i)\\ \mathscr{L}_2 &= \frac{1}{2\binom{N}{2}}\sum_{i=1}^{N}\left[\binom{i-1}{1} - \binom{N-i}{1}\right]X(i)\\ \mathscr{L}_3 &= \frac{1}{3\binom{N}{3}}\sum_{i=1}^{N}\left[\binom{i-1}{2} - 2\binom{i-1}{1}\binom{N-i}{1} + \binom{N-i}{2}\right]X(i)\\ \mathscr{L}_4 &= \frac{1}{4\binom{N}{4}}\sum_{i=1}^{N}\left[\binom{i-1}{3} - 3\binom{i-1}{2}\binom{N-i}{1} + 3\binom{i-1}{2}\binom{N-i}{2} + \binom{N-i}{3}\right]X(i),\end{aligned} \tag{4}$$

where $\binom{N}{k}$ is the binomial coefficient and X is arranged in an ascending order. As one can see, $\mathscr{L}_1$ is simply the sample average, $\mathscr{L}_2$ is a measure of scale, while the higher order $\mathscr{L}$-moments, $\mathscr{L}_3$ and $\mathscr{L}_4$, are used to define the measures of skewness and kurtosis. A MatLab code is available to compute these $\mathscr{L}$ moments for a stochastic sample (Bekker 2024). Hosking (1990) introduced non dimensional $\mathscr{L}$-moment ratios and defined $\mathscr{L}$-skewness ($\mathscr{L}_s$) and $\mathscr{L}$-kurtosis ($\mathscr{L}_k$) as, $\mathscr{L}_s = \mathscr{L}_3/\mathscr{L}_2$ and $\mathscr{L}_k = \mathscr{L}_4/\mathscr{L}_2$, respectively. Unlike the conventional statistical moments, $\mathscr{L}$-moment ratios are bounded so that $\mathscr{L}_s$ lies within $(-1, 1)$, and $\mathscr{L}_k$ within $(1.25\mathscr{L}_s^2 - 0.25, 1)$. Such bounds are considered an advantage because it is easier to interpret bounded measures than the conventional skewness and kurtosis moments, which can take arbitrarily large values. Another advantage of $\mathscr{L}$-moments is these are particularly well suited for the analysis of heavy-tailed distributions (without any exponential bounds) because, unlike the conventional moments, they are finite for all distributions that have finite means. Even for distributions with tails so heavy that the mean is infinite, $\mathscr{L}$-moments provide effective tools for statistical inference (Hosking 2007). As a point of reference, $\mathscr{L}_s$ and $\mathscr{L}_k$ for Gaussian distribution are 0 and 0.1226, while for an exponential one they are 0.3333 and 0.1667, respectively. For conventional product-based moments, the kurtosis values for Gaussian and exponential distributions are 3 and 6, respectively.

The heavy-tail distributions are fairly common across various disciplines. For example, Newman (2005) argues that the distributions of sizes of cities, earthquakes, forest fires, solar flares, moon craters, and personal fortunes all exhibit power-law behavior and thus fall into the category of heavy-tailed distribution. In turbulent flows, the heavy-tailed distributions appear when one considers the PDFs of the zero-crossing time scales or in other words, the persistence time scales. For instance, let us consider a sample turbulent signal of velocity fluctuations (u signal) from an atmospheric surface layer flow (Fig. 1a). In Fig. 1a, the zero-crossing points are denoted by the red crosses and the time between two successive crossings is denoted by t_p. The t_p can also be interpreted as the time scales of the positive

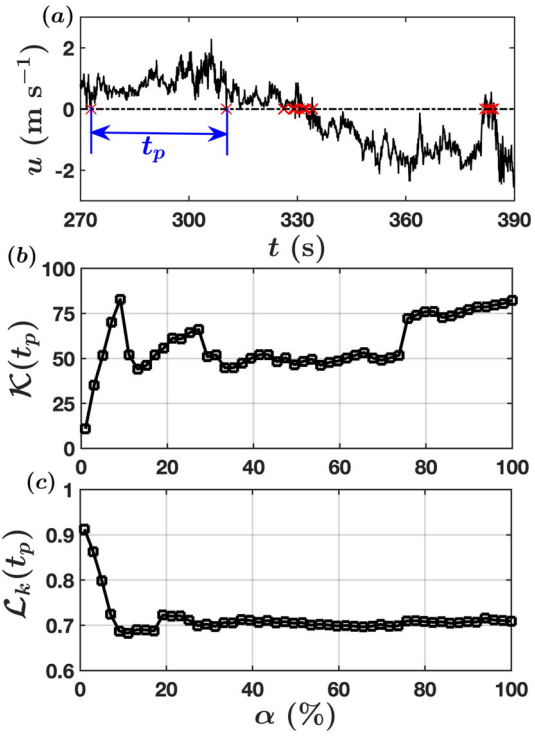

Fig. 1 **a** A sample time series of the streamwise velocity fluctuation (u) is shown, where t_p indicates the zero-crossing or persistence time scale while the red crosses represent the zero-crossing points. **b** The conventional kurtosis of t_p values ($\mathscr{K}(t_p)$) are shown by changing the percentage of zero-crossing samples (α) used for computation. **c** The same information is shown but for $\mathscr{L}$-kurtosis of t_p values ($\mathscr{L}_k(t_p)$)

and negative events, and can be written as $t_p = N_p/f_s$, where N_p is the event length and f_s is the sampling frequency. Note that N_p and t_p can be used interchangeably although unlike t_p, N_p is a discrete quantity. Notwithstanding these subtleties, if one plots the PDFs of t_p with a standard normalization, $(t_p - \overline{t_p})/\sigma_{t_p}$, where $\overline{t_p}$ and σ_{t_p} are the mean and standard deviation, and compare them with an equivalent Gaussian distribution, it can be clearly seen that these PDFs display quite a heavy tail (see Fig. S1b in the Supplementary Material). Such heavy tails are associated with large t_p values, often exceeding the integral scales and thus represent the coherent structures in atmospheric flows. These heavy tails arise because the PDFs of t_p display an extended power-law behavior with an exponential decay (Chamecki 2013; Chowdhuri et al. 2020).

An important statistical quantity to characterize these heavy tails is the kurtosis or the fourth-order moment. Typically, the computation of such higher-order moments requires large sample sizes to ensure statistical convergence. This is because the conventional kurtosis moments involve the fourth power of a stochastic signal, thereby giving more weight to the extremes that are poorly sampled when the sample space is small. This is particularly relevant for a stochastic signal such as t_p, for which the sample size is rather limited. For instance, considering a 30-min run sampled at a frequency of 20 Hz, the number of t_p samples would hardly be of the order of 1000. Therefore, to highlight this convergence issue, in Fig. 1b, we show the kurtosis of t_p, $\mathscr{K}(t_p)$ (see Eq. 2), after artificially reducing the number of t_p samples. This reduction is shown as a percentage of the original sample length and denoted as α. One can notice that the $\mathscr{K}(t_p)$ values suffer from convergence as they do not attain a plateau even when α reaches nearly 100%. On the other hand, if one plots $\mathscr{L}_k(t_p)$, computed from Eq. 4, quite fast convergence is achieved as the values become stable even at an α as

small as 20% (Fig. 1c). This establishes the superiority of the $\mathscr{L}$-kurtosis moments to quantify the heavy tails of the event length or persistence PDFs. It is, however, important to note that from both conventional and $\mathscr{L}$-moment perspectives, the PDFs of t_p remain largely different from an exponential one since $\mathscr{K}(t_p)$ and $\mathscr{L}_k(t_p)$ values significantly exceed 6 and 0.16667 respectively.

In general, the distribution of zero-crossing time scales is a non-trivial problem and poses serious theoretical challenges to derive them from the first principles (Majumdar 1999). Therefore, a bounded statistical measure such as $\mathscr{L}$-kurtosis to quantify these non-trivial distributions is of significant value. To associate these $\mathscr{L}$-kurtosis moments further with the underlying turbulence physics, we generate a scale-wise description of $\mathscr{L}_k(N_p)$ values. For convenience purposes, we use the event lengths N_p. The scale-wise description is achieved by computing the $\mathscr{L}_k(N_p)$ values of the velocity increment signals (for instance, Δu), which is defined as $u(t+\Delta t)-u(t)$, where Δt is the time lag. These time lags represent the eddy time scales in the flow. In the context of Δu, N_p represents the length of the events up to which Δu values stay either positive or negative.

For a turbulent boundary layer, Chowdhuri and Banerjee (2023) studied how the PDFs of N_p associated with the Δu signals evolved as the time lags Δt increased. They qualitatively demonstrated that when the Δt values were sufficiently large, the N_p PDFs of Δu signals could explain the long events found in the original u signals. We display their result in Fig. S2a of the Supplementary Material, where Δt values are scaled with the inner-layer variables and denoted as $\Delta t^+ = \Delta t u_*^2/\nu$. From Fig. S2a, one can infer that the heavy tails in the N_p PDFs of u signals are, in fact, caused by the passage of coherent structures in the flow. To quantify this behavior through the $\mathscr{L}$-moment framework, if one plots the $\mathscr{L}_k(N_p)$ values of Δu signals against Δt^+ ($\mathscr{L}_k^{\Delta u}$), at scales large enough they approach the $\mathscr{L}_k(N_p)$ values of u signals ($\mathscr{L}_k^u$, see Fig. S2b of the Supplementary Material). Therefore, the ratio $\mathscr{L}_k^{\Delta u}/\mathscr{L}_k^u$, reveals the role of the eddy motions towards generating the large events in a turbulent flow field. Henceforth, the scale-wise $\mathscr{L}_k(N_p)$ values will be denoted simply as, $\mathscr{L}_k^{\Delta u}$ and the $\mathscr{L}_k(N_p)$ values corresponding to the full signals will be written as, $\mathscr{L}_k^u$.

2.3 Wavelet Analysis

In addition to the $\mathscr{L}$-moment analysis, we carried out a wavelet analysis on the u and w signals to compute their cospectra and coherence spectra. As will be shown later (see Sect. 3), regarding canopy flows, the wavelet analysis provides some interesting observations, which are further explained through the $\mathscr{L}$-moment analysis. Therefore, these two different methods complement each other quite nicely.

For the wavelet analysis, we used 'Morlet' as the mother wavelet due to its localization properties. The wavelet scales were converted to equivalent Fourier frequencies (f), using the relationship provided by Torrence and Compo (1998). The premultiplied global wavelet cospectrum between u and w ($fS_{uw}(f)$) was defined as,

$$fS_{uw}(f) = \frac{\delta t}{N}\sum_{n=1}^{N}\mathscr{R}\left[\frac{W_n^u(s_j)\overline{W_n^w(s_j)}}{s_j}\right], \tag{5}$$

where s_j are the wavelet scales, $W_n^u(s_j)$ is the wavelet coefficient for the u signal at scale s_j, $\overline{W_n^w(s_j)}$ is the complex conjugate of the wavelet coefficient for the w signal at scale s_j, $\mathscr{R}$ is the real component of a complex number, N is the number of data points in a time series, J is the total number of scales, and δt is the sampling period, which is equal to $1/f_s$ with f_s

being the sampling frequency. Equation (5) can also be used to compute the spectra if instead of two different signals similar ones are used.

The coherence spectrum, on the other hand, is defined as,

$$\Gamma^2_{u,w}(f) = \frac{1}{N}\sum_{n=1}^{N} \frac{|\mathscr{R}(W^{uw}) + \mathscr{C}(W^{uw})|^2}{W^{uu}W^{ww}}, \tag{6}$$

where $\Gamma^2_{u,w}(f)$ is the squared coherence between u and w, $W^{xy} = W^x_n(s_j)\overline{W^y_n(s_j)}$ with x and y being equal to either u or w, and $\mathscr{R}$ and $\mathscr{C}$ are the real and imaginary components of a complex number. Henceforth, f will be removed from $\Gamma^2_{u,w}(f)$ while showing the results. The same procedure can be repeated to compute the squared coherence between any two signals.

We also conducted a wavelet cross-scalogram analysis on the u and w signals. Wavelet cross-scalograms include time information in addition to coherence and phase. We implemented this based on the MatLab code provided in Grinsted et al. (2004) with default choices such as: a mother wavelet of 'Morlet'; a scale resolution of 10 scales per octave; and the addition of zeros at the end to increase the length of the time series to the nearest power of 2. This artificial addition of zeros added a 'cone of influence', within which the results were not interpreted as they are impacted by the edge effects. The datasets (except the CAIPEEX ones) and codes used in this study are available at Chowdhuri (2024).

3 Results and Discussion

We begin by showing how the concept of $\mathscr{L}$-kurtosis can be effectively applied to gain valuable insights into RSL flows and highlight their differences with respect to ASL flows. In our analysis we specifically focus on the streamwise and vertical velocity fluctuations (u and w), since these two signals together explain the vertical momentum transport (uw) between the upper atmosphere and the canopy air space. These results are complemented with wavelet analysis, pointing towards how differently the canopy-scale coherent structures modulate the horizontal and vertical velocity components in sub-canopy environments. This is dissected further by first conditionally sampling the momentum fluxes into its gradient ($uw < 0$) and counter-gradient ($uw > 0$) components and later carrying out an $\mathscr{L}$-kurtosis analysis on their time scales. Contrary to ASL flows, for RSL ones, it is shown that the eddy processes responsible for the transport of momentum in the gradient and counter-gradient directions display different scaling properties. These results shed light on why the integral time scales of vertical velocity decrease with height in canopy sub-layers.

3.1 Contrast Between ASL and RSL Flows

Figure 2 depicts the scale-wise evolution of the $\mathscr{L}$-kurtosis ($\mathscr{L}_k$) values of the event lengths, corresponding to the Δu ($\mathscr{L}_k^{\Delta u}$) and Δw ($\mathscr{L}_k^{\Delta w}$) signals. Here, Δx (where $x = u, w$) are the velocity increments, defined as $\Delta x = x(t+\Delta t) - x(t)$, where Δt is the prescribed time lag. The time lags are normalized by the integral time scales of u (γ_u) or w (γ_w), depending on the signal types. As per the standard practice, the integral scales are computed by integrating the autocorrelation functions of the velocity signals up to their first zero-crossings (Chamecki 2013). The curves shown in Fig. 2 are ensemble averaged over all the near-neutral runs, and their run-to-run variations, expressed as one standard deviation from the ensemble

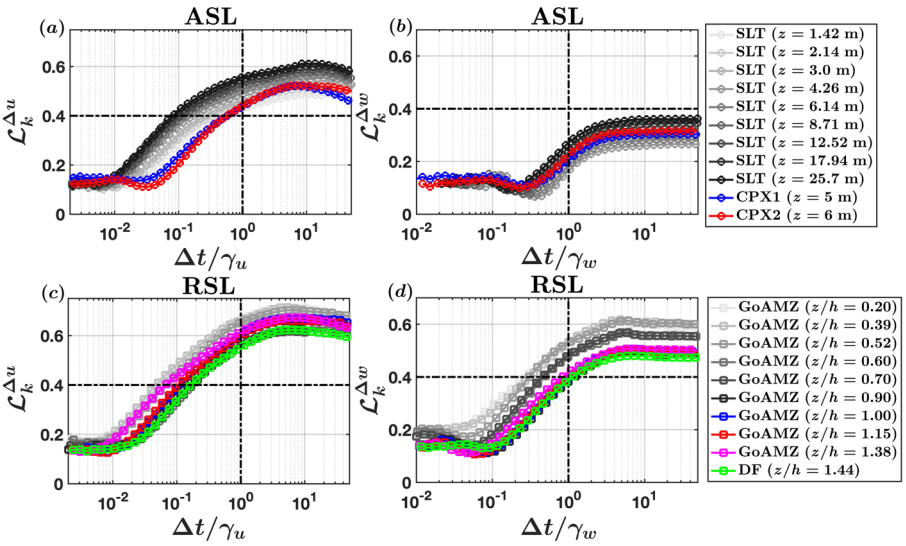

Fig. 2 The $\mathscr{L}$-kurtosis values of the event lengths are shown for the **a** Δu ($\mathscr{L}_k^{\Delta u}$) and **b** Δw ($\mathscr{L}_k^{\Delta w}$) signals, corresponding to ASL flows. Here, Δu and Δw represent the velocity increments at a time lag Δt. The time lags are normalized by the integral time scales of u and w, respectively (γ_u and γ_w). **c**, **d** In the bottom panels, the same information are shown but for the RSL flows. The legends at the right-hand side describe the different ASL and RSL datasets used in the present analysis. For brevity, SLTEST, GoAmazon, CAIPEEX, and Duke Forest datasets are labeled as SLT, GoAMZ, CPX (1,2), and DF, respectively. The horizontal dash-dotted lines denote the critical $\mathscr{L}$-kurtosis value of 0.4, beyond which the PDF-based moments cease to exist

mean, are found to be small in all the cases. The associated error-bar plots, corresponding to RSL flows, are shown as an example in Fig. S3 of the Supplementary Material. Throughout this study we use integral time scales rather than converting them to length scales through Taylor's hypothesis, since its applicability remains questionable in RSL flows.

The upper two panels in Fig. 2 show the plots from the ASL flows (Fig. 2a, b), while the bottom two panels show the same for the RSL flows (Fig. 2c, d). The multiple heights from the SLTEST and GoAmazon datasets are color-coded in gray shades with their intensities increasing as the heights increase. Regardless of the signal types, the $\mathscr{L}_k^{\Delta x}$ values monotonically increase with increasing time-lags and eventually attain a plateau at scales comparable to the integral scales. As shown in Appendix A, the $\mathscr{L}_k^{\Delta x}$ values associated with these plateaus are equal to $\mathscr{L}_k^{x}$, i.e. the values obtained from the event lengths (N_p) of the full signals. This signifies that at Δt values of the order of integral scales, the N_p PDFs of Δx signals fully explain the persistently long events found in the original x signals. In other words, the long-duration events in the velocity signals (either u or w) are formed when the larger-scales in the flow are accounted for. This mechanism is analogous to how the very-large-scale motions (VLSMs) are formed in the log-layers of wall-bounded flows, where it is argued that these VLSMs or long-duration motions are created by an accumulation of coherent structures in the flow (Deshpande et al. 2023). Coming back to Fig. 2, the attainment of a plateau at scales of the order of γ_x indicates that the heavy tails of the event length PDFs of u or w signals are clearly associated with the large-scale coherent structures being passed over the measurement location. Despite such similarities, clear differences appear between the ASL and RSL flows when the u and w signals are separately looked at.

For instance, one can notice nearly no discernible differences between the ASL and RSL flows when $\mathscr{L}_k^{\Delta u}$ curves are considered. For both of these flows, $\mathscr{L}_k^{\Delta u}$ curves cross 0.4 after a threshold time scale. The significance of $\mathscr{L}_k^{\Delta u} \geq 0.4$ comes from the literature of $\mathscr{L}$-moments, where it is postulated that the $\mathscr{L}$-kurtosis exceeding 0.4 indicates that the conventional PDF-based moments do not exist for a stochastic signal (Nair et al. 2022). This is interesting because the mean of the zero-crossing rate of a turbulent signal is associated with the dissipation rate of the turbulence kinetic energy (Sreenivasan et al. 1983; Poggi and Katul 2010). For future studies, it remains to be seen whether the $\mathscr{L}$-kurtosis values of the event lengths can be used to correct the dissipation rate estimates of the turbulence kinetic energy.

On the other hand, the $\mathscr{L}_k^{\Delta w}$ curves differ significantly between the ASL and RSL flows. From Fig. 2b, it is quite apparent that the $\mathscr{L}_k^{\Delta w}$ values remain considerably smaller than 0.4 at all scales of the flow. Conversely, for the RSL flows, similar to $\mathscr{L}_k^{\Delta u}$, $\mathscr{L}_k^{\Delta w}$ values exceed 0.4. This indicates that the PDFs of the event lengths are heavier than the ASL flows, thereby signifying more coherence in w signals of RSL flows as compared to a canonical atmospheric surface layer. Moreover, the $\mathscr{L}_k^{\Delta w}$ curves of RSL flows separate from one another as the heights approach the canopy top indicative that long events are more prevalent in w time series close to the forest floor than higher up. These discrepancies get further highlighted when one plots the time-height contours of $\mathscr{L}_k^{\Delta x}$ values (Fig. 3a, b).

In Fig. 3a, b the information presented in Fig. 2 is shown in the form of contour plots. In comparison to line plots, the contour representation of $\mathscr{L}_k^{\Delta x}$ values is more beneficial to differentiate better between the ASL and RSL flow features. The x axes of Fig. 3a, b denote the normalized time lags, while the y axes represent the standardized heights. For this purpose, only the SLTEST and GoAmazon datasets are used to represent the ASL and RSL flows, respectively, since they contain multi-level measurements. Given their different height ranges, the z values are scaled as $(z - z_{\min})/(z_{\max} - z_{\min})$. In this scaled coordinate system, the canopy top appears at a value of around 0.75, which is shown as a dash-dotted horizontal line in Fig. 3a, b. Moreover, as the ranges of $\mathscr{L}_k^{\Delta x}$ values also differ between the two datasets (Fig. 2), they are normalized by their full signal values and therefore remain bounded between 0 to 1 (see Fig. 8 in Appendix A). The contours associated with the ASL and RSL datasets are identified by different colors and line types, blue (dash-dotted lines) and red (solid lines), respectively.

After carrying out these exercises, one can notice the striking similarities between the blue and red contours of the u signals in Fig. 3a. In fact, except the lowest few levels, the contours of $\mathscr{L}_k^{\Delta u}/\mathscr{L}_k^{u}$ agree remarkably well between the ASL and RSL flows at all time scales. Since the streamwise velocity fluctuations are more influenced by the eddies whose sizes scale with the atmospheric boundary layer (ABL) depth, this finding underscores the importance of the ABL-scale motions for both ASL and RSL flows (Dupont and Patton 2022). On the contrary, the blue and red contour lines of $\mathscr{L}_k^{\Delta w}/\mathscr{L}_k^{w}$ clearly differ from one another at heights $(z - z_{\min})/(z_{\max} - z_{\min}) < 0.75$ (within the canopy), albeit they match well for heights above the canopy. Therefore, these findings indicate that the dynamics of the vertical velocity fluctuations encode the effects of canopy-scale eddies in RSL flows, which is a specific feature of canopy turbulence only. We next perform a wavelet analysis to lend more credence to this.

To determine whether the canopy-scale eddies indeed act differently on the streamwise and vertical velocity fluctuations, we carried out a wavelet coherence analysis on the GoAmazon dataset. In this analysis, the squared wavelet coherence ($\Gamma^2_{x,x_{\text{ref}}}$, $x = u, w$) was computed between the two signals, where the reference signal (x_{ref}) was located exactly at the canopy

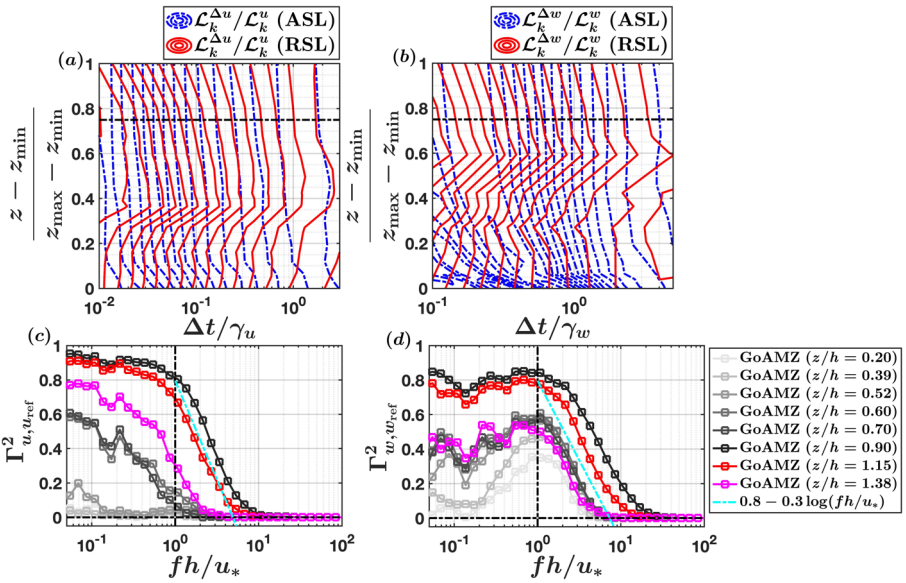

Fig. 3 The time-height contour plots of **a** $\mathscr{L}_k^{\Delta u}$ and **b** $\mathscr{L}_k^{\Delta w}$ are shown to compare the features between the ASL and RSL flows. For this purpose, the SLTEST and GoAmazon datasets are used to represent the ASL and RSL flows, respectively. Note that the $\mathscr{L}_k^{\Delta x}$ ($x = u, w$) are normalized with the $\mathscr{L}_k$ values of the event time scales as obtained from the full-signals ($\mathscr{L}_k^x$). The heights (z) are scaled as $(z - z_{\min})/(z_{\max} - z_{\min})$. The contours are spaced in the increments of 0.05 for both ASL and RSL datasets. Corresponding to RSL flows, the wavelet-based coherence spectra are shown for **c** u and **d** w signals, where $\Gamma^2_{x,x_{\mathrm{ref}}}$ represents the squared coherence between the x and x_{ref} signals. Here, x_{ref} indicates the reference signals exactly at the canopy top ($z/h = 1$) while the x signals are from heights other than that. The frequencies are normalized by the canopy time scale (fh/u_*) and the vertical dash-dotted lines in (**c**) and (**d**) denote the position $fh/u_* = 1$. The cyan dash-dotted lines in (**c**) and (**d**) indicate the logarithmic scaling of the coherence spectra, commonly found for ASL flows (Li et al. 2024). The h denotes the canopy height while u_* is the friction velocity at the canopy top. The different heights from the GoAmazon dataset are shown in the legend

top ($z/h = 1$) while the other ones (x) were sampled from rest of the heights. Physically, the squared coherence estimates indicate how strongly the two signals are linearly correlated with each other at each frequency (Thomson and Emery 2014). For this purpose, the 'Morlet' wavelet was chosen as the mother wavelet and the frequencies (f, converted from wavelet scales) were scaled with the canopy time scale h/u_*. The procedure to compute this coherence is same as shown in Eq. (6). Note that the quantity h/u_* is height-invariant and therefore can be considered as a global time scale (Brunet 2020).

By comparing the scale-wise behavior of $\Gamma^2_{u,u_{\mathrm{ref}}}$ with $\Gamma^2_{w,w_{\mathrm{ref}}}$, it is conspicuous that the $\Gamma^2_{w,w_{\mathrm{ref}}}$ curves attain a clear peak at a time scale of $fh/u_* = 1$ for all the z values (Fig. 3d). On the other hand, the $\Gamma^2_{u,u_{\mathrm{ref}}}$ curves remain close to zero for the lowest three heights of the GoAmazon dataset (Fig. 3c). In fact, similar outcomes are obtained, if instead of a coherence analysis, a lead-lag correlation analysis were carried out with the reference signals being located at the canopy top. Thereby, these findings can be considered to be robust while raising an important point. If the u signals are considered solely, then one might interpret that the canopy-scale eddies only exert their influences up to a certain height since the lowest three levels appear to be disconnected with the turbulent processes occurring at the canopy top. The same conclusion does not hold in the case of w signals, for which the influences of

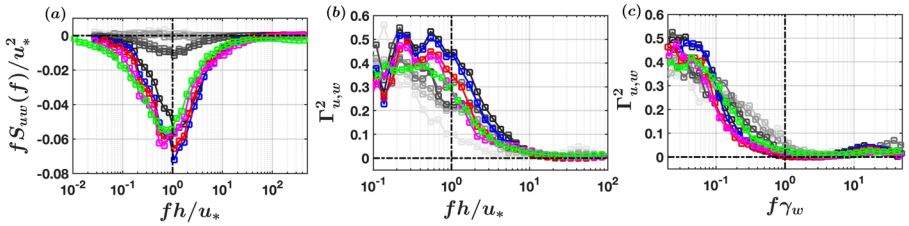

Fig. 4 For the RSL flows, the wavelet-based **a** premultiplied cospectra ($fS_{uw}(f)$) and **b** coherence spectra ($\Gamma^2_{u,w}$) are shown between the u and w signals. The cospectral amplitudes are normalized by u_*^2 and the frequencies (f) are normalized by the canopy time scale. The vertical dash-dotted lines in (**a**) and (**b**) denote the position $fh/u_* = 1$. **c** The same coherence spectra between u and w signals are shown but the frequencies are normalized with the integral time scale of the w signal (γ_w). Different colors represent the two different RSL datasets as shown in the legend of Fig. 2c, d

the canopy eddies can even be felt at those lowest three heights. However, the coefficients $\Gamma^2_{u,u_{\text{ref}}}$ or $\Gamma^2_{w,w_{\text{ref}}}$ only reveal the strength of linear relationships at each scale of the flow (Thomson and Emery 2014) and this limitation should be accounted for while interpreting the results (see the discussion in Sect. 4).

In the context of ASL flows, the attached eddy hypothesis dictates that the squared coherence coefficients follow a logarithmic scaling with the wavenumbers (Li et al. 2024). On a semi-log coordinate system, this scaling appears as a straight line. For the RSL flows, similar logarithmic scalings are observed in $\Gamma^2_{u,u_{\text{ref}}}$ and $\Gamma^2_{w,w_{\text{ref}}}$, as shown by the cyan dash-dotted lines in Fig. 3c, d. Here, we use the expression $C_1 \log(fh/u_*) + C_2$ to represent this logarithmic scaling, where C_1 and C_2 are -0.3 and 0.8, respectively (Li et al. 2024). For the u component, the logarithmic scaling is only clearly visible for heights close to or above the canopy top ($z/h \geq 0.9$, Fig. 3c), while for w it extends all the way to heights deep within the canopy (Fig. 3d).

Regarding ASL flows, the squared coherence information is used to estimate the footprints of large-scale structures from the velocity signals measured at heights close to the surface (linear stochastic estimation). For RSL flows, the same procedure to extract the effects of canopy-scale structures from sub-canopy velocity signals only appear to be possible for the vertical velocity component. Since the vertical velocity fluctuations are the dominant carriers of momentum across the atmosphere and the canopy air space, we next investigate the impact of these canopy-scale eddies on the momentum transport in RSL flows.

3.2 Momentum Transport in RSL Flows

Figure 4a shows the premultiplied wavelet cospectra ($fS_{uw}(f)$) between the u and w signals for the RSL flows. The corresponding u and w spectra are shown in Fig. S4 of the Supplementary Material. As usual, the frequencies are normalized with the canopy time scale and the cospectral amplitudes are scaled by the square of the friction velocity at the canopy top. The cospectral amplitudes decrease rapidly towards zero as measurement height decreases below $z = h$, since most of the momentum is absorbed by the upper parts of the canopy. For heights above the canopy, the cospectral amplitudes show a clear peak at a scaled frequency commensurate with $fh/u_* = 1$ albeit slight height dependence is observable.

As opposed to the cospectral amplitudes, if one investigates the squared coherence between the u and w signals, the $\Gamma^2_{u,w}$ values remain somewhat larger than zero even for heights deep within the canopy, especially at frequencies $fh/u_* \leq 1$ (Fig. 4b). Note that in Fig. 4b the

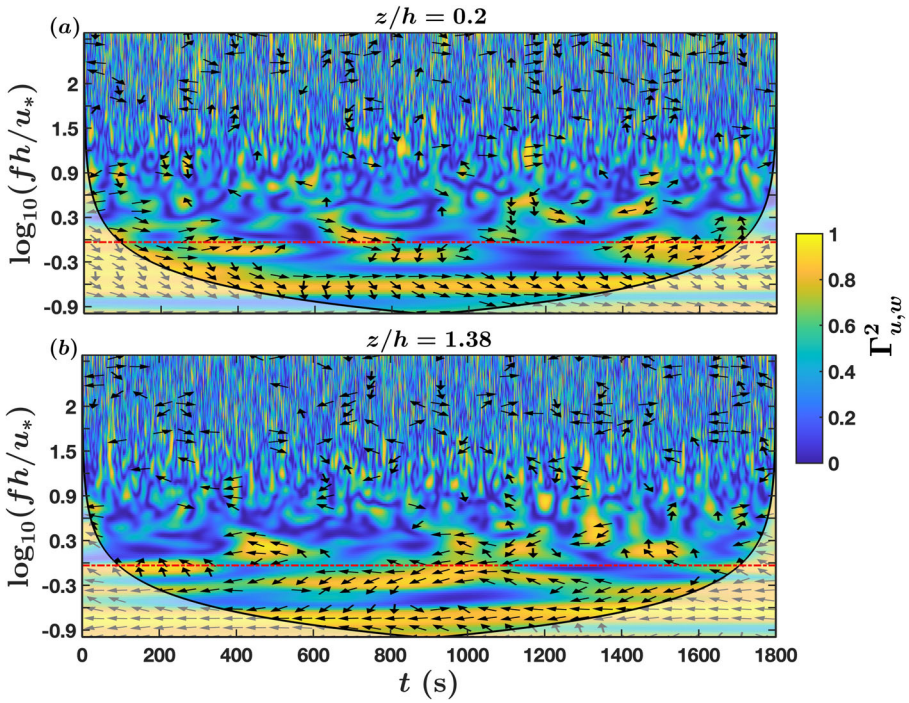

Fig. 5 The wavelet cross-scalograms between u and w signals are shown for a specific 30-min run from the GoAmazon dataset, corresponding to the measurement levels **a** $z/h = 0.2$ and **b** $z/h = 1.38$. The colored contours represent the squared coherence $\Gamma^2_{u,w}$ (see the color bar) while the vertical and horizontal axes denote the scaled frequencies ($\log_{10}(fh/u_*)$) and time instants (t in seconds), respectively. The arrows show the direction of the momentum transfer and the black curved lines represent the cone-of-influence, beyond which the $\Gamma^2_{u,w}$ values cannot be trusted. The horizontal red dash-dotted line indicates $fh/u_* = 1$

range of x-axis begins from $fh/u_* \geq 0.1$, and the purpose of this is not to show the noisy $\Gamma^2_{u,w}$ values at very low frequencies. Nevertheless, the non-zero $\Gamma^2_{u,w}$ values indicate that the canopy-scale eddies insert their influences at heights deep within the canopy, although they do not transport any momentum in an averaged sense at heights $0.2 \leq z/h \leq 0.7$. However, it is not solely the canopy-scale eddies that dictate the behavior of the coherence curves. In fact, these curves can be collapsed reasonably well if the integral time scale of the vertical velocity fluctuations is used in place of the canopy time scale (Fig. 4c). Under such scaling, the non-zero values of $\Gamma^2_{u,w}$ only extend up to frequencies $f\gamma_w < 1$ (Fig. 4c). These observations from Fig. 4 raise an important question, i.e. at heights within the canopy ($0.2 \leq z/h \leq 0.7$), what physical processes govern the non-zero $\Gamma^2_{u,w}$ values (at frequencies $fh/u_* < 1$ or $f\gamma_w < 1$) despite the cospectral amplitudes being nearly zero?.

To provide a definitive answer to this, we investigate the wavelet cross-scalograms between the u and w signals for a specific 30-min run from the GoAmazon dataset (Fig. 5). These cross-scalograms are computed using the procedure described by Grinsted et al. (2004) and we only show them for two measurement levels, one at a $z/h = 0.2$ (Fig. 5a) and the other at a $z/h = 1.38$ (Fig. 5b). The conclusions remain the same if any other measurement heights or 30-min runs were used in the analysis. In these diagrams, the contours represent the squared coherence $\Gamma^2_{u,w}$, while the horizontal and vertical axes denote the time-instants (t in seconds) and the logarithm values of the scaled frequencies ($\log_{10}(fh/u_*)$). These frequencies are

converted from the wavelet periods and thereafter scaled with the canopy time scale. The arrows depict the phase information between the u and w signals and are shown only for those coherence values that are statistically significant. If the arrows point towards right, then it means the u and w signals are in phase, or in other words, the uw values are positive. Conversely, when the arrows point towards the left, they indicate that the u and w signals are out of phase with the uw values being negative. No momentum is transported when the arrows are vertically up or down since the phase angles in such cases remain at either 90° or 270°. According to the quadrant nomenclature (Wallace 2016), positive uw values belong to the counter-gradient quadrants (outward- and inward-interaction) while the negative ones belong to the gradient quadrants (ejection and sweep).

From Fig. 5a one can see that the coherence values at larger time scales ($fh/u_* < 1$) of the flow are mostly associated with the phase arrows pointing towards the right. Therefore, at within canopy levels, the non-zero values of $\Gamma^2_{u,w}$ are associated with the counter-gradient momentum transport events. The situation reverses for heights above the canopy (Fig. 5b), where the large coherence levels coincide with the gradient momentum transport (arrows pointing towards the left). The abundance of the counter-gradient momentum events, occurring at heights $z/h < 1$, is also reflected in the PDFs of event lengths, computed separately for each of the four quadrants (see Fig. S5 in the Supplementary Material).

3.3 Positive and Negative Flux Events

The PDFs of event lengths, corresponding to the counter-gradient quadrants, clearly display heavy tails at larger time scales for heights $z/h < 1$ (Fig. S5c, d). However, these heavy tails disappear progressively as the heights approach the canopy top. On the other hand, the event length PDFs of the gradient quadrants remain remarkably invariant with height (Fig. S5a, b). Therefore, it is apparent that the coherent structures inside the canopy air space comprise both of counter-gradient and co-gradient events.

To investigate this further, we first conditionally sample the positive and negative momentum flux events at each scale of the flow. At a time lag of Δt, the positive momentum flux events are represented as $\Delta u \Delta w > 0$ while the negative ones are $\Delta u \Delta w < 0$. In Fig. 9 of Appendix B, we illustrate why the $\Delta u \Delta w > 0$ and $\Delta u \Delta w < 0$ signals can be associated with counter-gradient and gradient transport at each scale of the flow. In Fig. 6a, b, we plot the $\mathscr{L}_k$ values of their event lengths, separately for the negative ($\mathscr{L}_k^{\Delta u \Delta w<0}$) and positive ($\mathscr{L}_k^{\Delta u \Delta w>0}$) components. Here, the time lags Δt are normalized by the canopy time scale. Compared to Fig. 6b, from Fig. 6a it is conspicuous that the $\mathscr{L}_k^{\Delta u \Delta w<0}$ curves show weaker variations with height. Notwithstanding that the average momentum fluxes within the canopy are nearly zero (see Fig. 4a), this finding suggests that the ejection and sweep motions in the canopy sub layers carry the signatures of the mixing layer eddies although they do not actively transport any momentum.

Conversely, a strong height dependence is noted for $\mathscr{L}_k^{\Delta u \Delta w>0}$ curves at time scales beyond $\Delta t u_*/h = 0.05$. In the frequency domain, the time scale $\Delta t u_*/h = 0.05$ is converted to $fh/u_* = 20$, which roughly corresponds to the beginning of the inertial subrange in the velocity spectra (see Fig. S4 in the Supplementary Material). Beyond $\Delta t u_*/h = 0.05$, the values of $\mathscr{L}_k^{\Delta u \Delta w>0}$ remain significantly higher for the heights within the canopy, with the largest values typically being found at the lowest three levels. Accordingly, the plateaus attained by the $\mathscr{L}_k^{\Delta u \Delta w>0}$ curves also show a similar behavior. Therefore, one is more likely to encounter long lasting counter-gradient events near the forest floor rather than at the higher heights. Statistically speaking, we can thus conclude that within the canopy air space

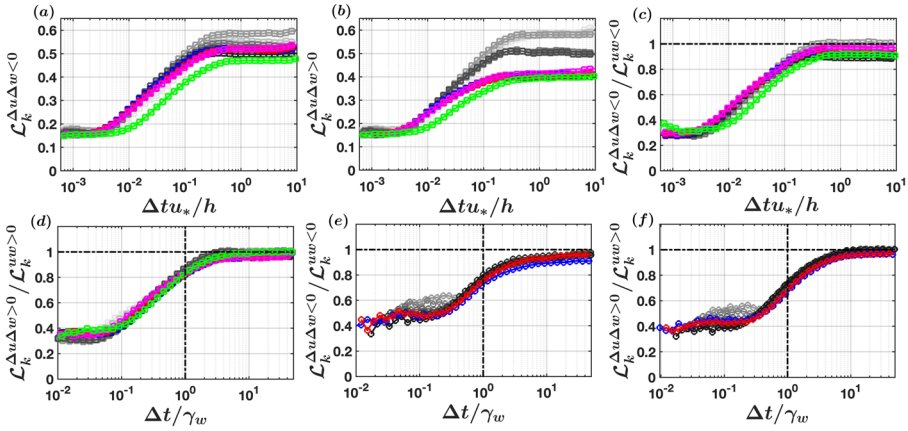

Fig. 6 For the RSL datasets, the scale-wise evolution of the $\mathscr{L}_k$ values of the event lengths are shown separately for the **a** gradient ($\mathscr{L}_k^{\Delta u \Delta w<0}$) and **b** counter-gradient ($\mathscr{L}_k^{\Delta u \Delta w>0}$) momentum transport. The time-lags (Δt) are normalized by the canopy time scale. **c**, The $\mathscr{L}_k^{\Delta u \Delta w<0}$ values are plotted similarly as in (**a**) but those are scaled by the full-signal values, i.e. $\mathscr{L}_k^{uw<0}$. The $\mathscr{L}_k^{uw<0}$ values are obtained after conditionally sampling the negative instantaneous uw signals and computing the $\mathscr{L}_k$ values of their time scales. **d** A similar exercise is repeated for the counter-gradient momentum transport but the time-lags in that case are normalized by γ_w. For comparison purposes, in **e**, **f** the scaled curves are shown from the ASL datasets (SLTEST and CAIPEEX) by separating the momentum transport into its gradient and counter-gradient components. For both **e** and **f**, the time-lags are normalized by γ_w

the lengths of the counter-gradient events decrease with height. All these observations from Fig. 6a, b are consistent with the event length PDFs being presented in Fig. S5.

The differences between the positive and negative flux events are illustrated quite nicely in Fig. 10 of Appendix C. Now, the $\mathscr{L}_k^{\Delta u \Delta w<0}$ curves can be collapsed even better if the $\mathscr{L}_k^{\Delta u \Delta w<0}$ values are scaled by their full signal values, i.e. $\mathscr{L}_k^{uw<0}$ (Fig. 6c). The $\mathscr{L}_k^{\Delta u \Delta w>0}$ curves, on the other hand, collapse remarkably well when the time scales are normalized by the integral time scale of the vertical velocity (γ_w) and the $\mathscr{L}_k^{\Delta u \Delta w>0}$ values are scaled by $\mathscr{L}_k^{uw>0}$ (Fig. 6d). In fact, in these scaled coordinate systems, the two RSL datasets (GoAmazon and Duke forest) agree quite strongly with each other. The collapse is however poor for the $\mathscr{L}_k^{\Delta u \Delta w>0}/\mathscr{L}_k^{uw>0}$ curves if the time lags were scaled either by γ_u or the canopy time scale (see Fig. S6 in the Supplementary Material). The existence of two different time scales to collapse the event lengths of negative and positive momentum flux events is not applicable for atmospheric surface layer flows, since in those cases γ_w appears to be the only relevant time scale (Fig. 6e, f).

In a nutshell, these results suggest that the transport of gradient and counter-gradient momentum inside the canopy air space is accomplished through two different eddy processes. The gradient momentum exchanges occur at a time scale commensurate with the canopy time scale (h/u_*). However, for counter-gradient momentum exchanges, γ_w emerges to be the suitable scale. This result is in contrast with Chamecki (2013), who showed that the integral scales in canopy flows were related to the sweep events, i.e. the events responsible for gradient momentum exchanges. To reach this conclusion, Chamecki (2013) fitted exponential distributions to the tails of the persistence PDFs of $w < 0$ signals and used that information to define alternate time scales. These scales were eventually compared with the integral time scales. The analysis of Chamecki (2013) hinged on the observation that the tails of persistence

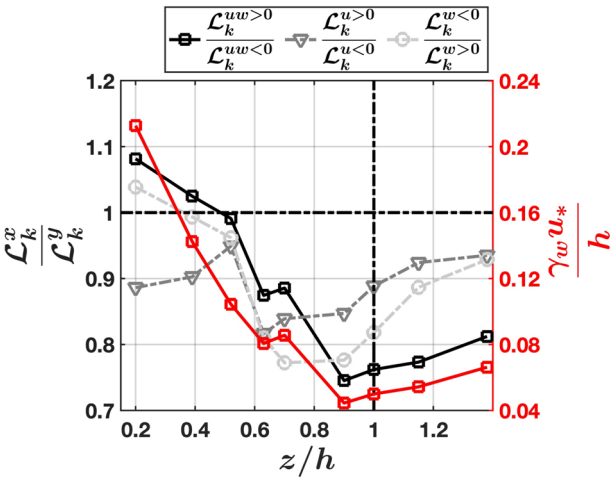

Fig. 7 For the GoAmazon dataset, the ratios $\mathscr{L}_k^{uw>0}/\mathscr{L}_k^{uw<0}$, $\mathscr{L}_k^{u>0}/\mathscr{L}_k^{u<0}$, and $\mathscr{L}_k^{w<0}/\mathscr{L}_k^{w>0}$ are plotted against the heights scaled by the canopy height. On the right hand side of y-axis, the normalized integral time scales of vertical velocity fluctuations ($\gamma_w u_*/h$) are shown. The legend on top indicates the different $\mathscr{L}$-moment ratios

PDFs of u and w signals differed between their positive and negative counterparts. Since $\mathscr{L}$-kurtosis can quantify the behavior of the PDF tails, we compare the following $\mathscr{L}$-kurtosis ratios, $\mathscr{L}_k^{uw>0}/\mathscr{L}_k^{uw<0}$, $\mathscr{L}_k^{u>0}/\mathscr{L}_k^{u<0}$, and $\mathscr{L}_k^{w<0}/\mathscr{L}_k^{w>0}$, for the GoAmazon dataset (Fig. 7).

From Fig. 7, it is obvious that the ratio $\mathscr{L}_k^{uw>0}/\mathscr{L}_k^{uw<0}$ (solid black line with square markers) mimics the behavior of γ_w (solid red line with square markers) the best. At the same time, the other two ratios ($\mathscr{L}_k^{u>0}/\mathscr{L}_k^{u<0}$ and $\mathscr{L}_k^{w<0}/\mathscr{L}_k^{w>0}$) show a weaker correspondence with γ_w. As compared to the gradient events, the time scales of counter-gradient ones show a strong variation with height (Fig. S5). Therefore, the height variations observed in the ratio $\mathscr{L}_k^{uw>0}/\mathscr{L}_k^{uw<0}$ are more influenced by the changes in $\mathscr{L}_k^{uw>0}$ values rather than in $\mathscr{L}_k^{uw<0}$. In other words, the correspondence between $\mathscr{L}_k^{uw>0}/\mathscr{L}_k^{uw<0}$ and γ_w is mainly determined by the counter-gradient events. This reinforces the observations from Fig. 6b and d, where γ_w emerged to be the suitable scale for counter-gradient momentum exchanges. The decrease of γ_w with height is not true for ASL flows, where the γ_w values are supposed to increase with height as a consequence of the attached-eddy hypothesis (see Fig. S7 of the Supplementary Material). It appears that any disagreements with Chamecki (2013) can possibly be resolved by recasting the observations from that study through the lens of $\mathscr{L}$-moment framework, which remains a topic for subsequent studies. We present our conclusions and future outlooks in the next section.

4 Conclusion

In this study, we developed an $\mathscr{L}$-moment based event framework to model the dynamics of a homogeneous canopy flow. Primarily, this study attempts to answer a few fundamental issues in canopy turbulence, which are: up to what depth do the canopy-scale eddies penetrate, what causes γ_w to decrease with height, and how exactly the canopy time scales and γ_w characterize the momentum transport in canopy flows?

To answer these questions, we considered the turbulent fluctuations at each scale of the flow to consist of an alternating positive and negative event chronicle with certain sizes. The PDFs of these event lengths become progressively heavy-tailed as the scales increase due to the presence of coherent structures in turbulent flows. The conventional statistical moments cannot quantify these heavy-tailed distributions, since those estimates do not converge satisfactorily at all. In that respect, the $\mathscr{L}$-moments are more useful, as these moments were specifically developed to deal with heavy-tailed distributions. Accordingly, the statistical distribution of these event lengths could be accounted for by computing their $\mathscr{L}$-kurtosis values, which quantify the heaviness of their tails. Therefore, the $\mathscr{L}$-moments allow us to reliably represent the event-length distributions, whose PDFs have non-trivial shapes with an extended power-law regime. Such metrics suitable for analyzing heavy-tailed distributions could be useful also for wind-energy applications where varying periods of constant wind speeds are known to affect the performance of the wind turbines. The insights obtained from this framework are complemented with a wavelet analysis.

Our results from coherence analysis indicate that the dynamics of the vertical velocity fluctuations encode the effects of canopy-scale eddies in RSL flows. Contrary to some previous literature, we propose that these canopy-scale eddies alter the flow deep within the canopy. This is by virtue of large $\Gamma^2_{w,w_{\mathrm{ref}}}$ values being found at heights deep within the canopy. Regarding the horizontal velocity fluctuations, no appreciable influence of canopy-scale eddies is found for the lowest three heights within the Amazon canopy ($0.2 \leq z/h \leq 0.5$), owing to near-zero values of $\Gamma^2_{u,u_{\mathrm{ref}}}$. At first glance, one might infer that the canopy-scale eddies do not modulate the sub-canopy horizontal flow field as strongly as the vertical one. However, it is important to take cognizance of the fact that the squared coherence coefficients only reveal the strength of linear relationships at each scale of the flow (Thomson and Emery 2014). By borrowing some advanced non-linear analysis tools of Chowdhuri and Banerjee (2024), our preliminary analysis provides evidence that the canopy-scale structures do modulate the sub-canopy horizontal flow field but through non-linear interactions, not accounted for in linear coherence analysis (not shown). This is especially true for the lowest three heights from the GoAmazon dataset. Since the instantaneous momentum flux signals are a product of horizontal and vertical velocity fluctuations, it is plausible that the differing influences of canopy-scale eddies on u and w components cause the discrepancies between the gradient and counter-gradient momentum exchanges in RSL flows.

Specifically, for counter-gradient momentum exchanges, γ_w emerges to be the suitable scale. Furthermore, the dynamics of vertical velocity fluctuations in sub-canopy flows can be largely explained through linear relationships associated with w at canopy top (Fig. 3d). By combining these two insights, we hypothesize that the existence of large counter gradient events in sub-canopy environments is a consequence of linear effects of canopy-scale eddies on within-canopy vertical velocity fluctuations. Here, linearity implies that a linear stochastic estimation technique (Li et al. 2024) can be used to extract the signatures of canopy-scale eddies from vertical velocities measured within the canopy. It remains to be seen whether the negative momentum events within the sub-canopy air space can be explained through the non-linear effects of canopy-scale eddies on the horizontal flow field. Therefore, for future studies, it is important to develop tools that can separately consider the linear and non-linear effects of canopy scale eddies transferred to the sub-canopy horizontal and vertical velocity fluctuations. In that regard, complex networks could be a suitable choice.

Moreover, our results provide a benchmark to test if the large-eddy simulation (LES) models of canopy flows can capture these nuances of momentum exchange processes occurring within the sub-canopy environments. This indeed has profound implications towards modeling the fire spread through a forest or the transportation of gases or bio-aerosol particles

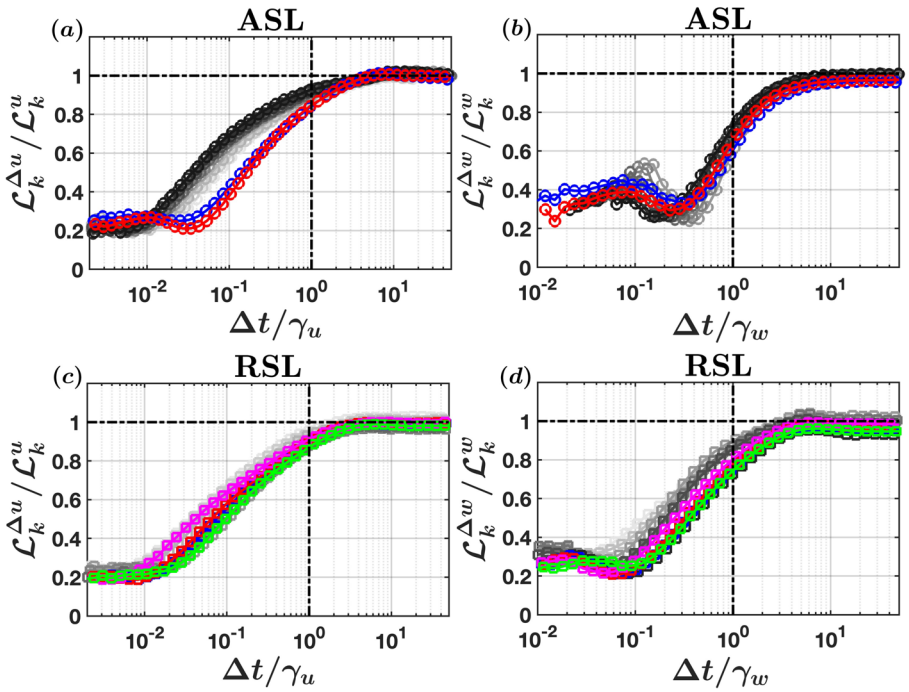

Fig. 8 Same as in Fig. 2, but the scale-wise $\mathscr{L}_k$ values ($\mathscr{L}_k^{\Delta x}$) are normalized by their respective full-signal values

emitted from the forest to the upper atmosphere. An another future direction is to investigate the role of heterogeneity (e.g., sparse canopies and canopy edge flows) and atmospheric stability on the scales of momentum transport and scalars, such as heat and moisture. Such alterations to canopy structure are often caused by forest management practices, such as clear-cutting or thinning. What remains unclear is how cutting down the trees, thereby reducing the leaf area density, would affect the interaction between the canopy- and γ_w-scale eddies. This has far-reaching implications towards designing mitigation strategies to constrain the spread of wildfires through a forest.

A Normalized $\mathscr{L}_k$ Curves

In this appendix, we show the scale-wise evolution of the $\mathscr{L}_k^{\Delta x}$ ($x = u, w$) values, corresponding to the event lengths of the Δx signals at a prescribed time lag Δt. As opposed to Fig. 2, instead of presenting the $\mathscr{L}_k^{\Delta x}$ values alone, we divide those with the $\mathscr{L}_k$ values obtained from the event lengths of the full signal x ($\mathscr{L}_k^{x}$). Under such normalization, one can notice from Fig. 8 that as the time lags increase, the $\mathscr{L}_k^{\Delta x}$ values approach $\mathscr{L}_k^{x}$, regardless of the signal or the flow types.

Notably, only for the ASL flows, there exist clear differences between the SLTEST and CAIPEEX datasets when the u signals are considered (Fig. 8a), a feature not immediately apparent from Fig. 2a. The zero-crossing properties of the u signals are influenced by the presence of the large-scale structures in the flow (Fig. 3a). Since these large-scale structures

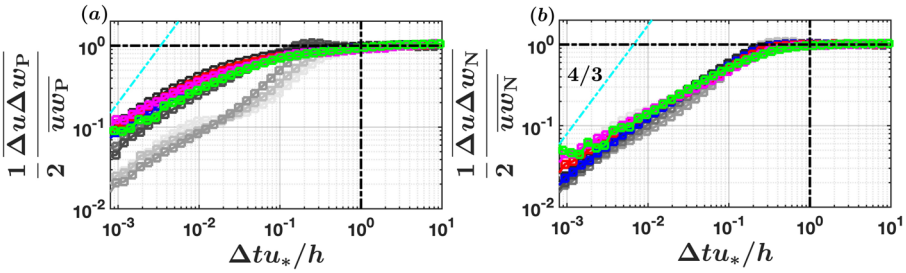

Fig. 9 For the RSL datasets, the structure function representation of the momentum fluxes are shown separately for the **a** positive ($\overline{\Delta u \Delta w_{\mathrm{P}}}$) and **b** negative ($\overline{\Delta u \Delta w_{\mathrm{N}}}$) components. The cyan dash-dotted lines indicate the 4/3 scaling of the momentum fluxes in the inertial subrange. The $\overline{uw_{\mathrm{P}}}$ and $\overline{uw_{\mathrm{N}}}$ denote the time-averaged positive and negative momentum flux contributions. The time lags are normalized by the canopy time scale

are sensitive to the boundary conditions, we attribute the differences in $\mathscr{L}_k^{\Delta u}/\mathscr{L}_k^{u}$ curves to the varying surface conditions at the SLTEST and CAIPEEX sites. However, for the w signal, we do not observe any such discrepancies as the curves collapse reasonably well among different datasets (Fig. 8b).

Nevertheless, the $\mathscr{L}_k^{\Delta w}/\mathscr{L}_k^{w}$ curves attain their plateaus at scales significantly larger γ_w (Fig. 8b). This is more obvious for the ASL flows rather than for the RSL (Fig. 8b and d). As discussed in Sect. 3.1, this difference is intimately linked to how the dynamics of the vertical velocity fluctuations encode the effects of canopy-scale eddies in RSL flows, a mechanism not applicable for ASL flows.

B Conditional Structure Functions of Momentum Flux

As an alternative to cospectral analysis, the scale wise contributions to turbulent momentum flux can also be studied via the mixed-order structure function, i.e. $\Delta u \Delta w$ (Chamecki et al. 2017; Ghannam et al. 2018). In fact, by expanding $\Delta u \Delta w$ and taking an average, one could write,

$$\begin{aligned}\overline{[u(t+\Delta t)-u(t)][w(t+\Delta t)-w(t)]} &= \overline{u(t+\Delta t)w(t+\Delta t)} \\ &+\overline{u(t)w(t)} - \overline{u(t+\Delta t)w(t)} - \overline{u(t)w(t+\Delta t)},\end{aligned} \tag{7}$$

As Δt approaches the integral scales (γx) of the flow, the last two terms from the right hand side of Eq. (7) disappear while the terms $\overline{u(t+\Delta t)w(t+\Delta t)}$ and $\overline{u(t)w(t)}$ both approach $\overline{uw}$ (Chamecki et al. 2017). Hence, at $\Delta t \to \gamma x$, $\overline{\Delta u \Delta w} \to 2\overline{uw}$. A consequence of this is, at any Δt, $\overline{\Delta u \Delta w}/2$ represents the cumulative contributions to the time-averaged momentum flux from scales smaller or equal to Δt (Chamecki et al. 2017; Ghannam et al. 2018).

Now, the time-averaged momentum flux $\overline{uw}$, can be written as a sum of gradient ($\overline{uw_{\mathrm{N}}}$) and counter-gradient ($\overline{uw_{\mathrm{P}}}$) contributions, expressed as $\overline{uw} = \overline{uw_{\mathrm{N}}} + \overline{uw_{\mathrm{P}}}$. Similar to $\overline{uw}$, the quantity $\overline{\Delta u \Delta w}$, can also be expressed as $\overline{\Delta u \Delta w} = \overline{\Delta u \Delta w_{\mathrm{P}}} + \overline{\Delta u \Delta w_{\mathrm{N}}}$. For either $\Delta u \Delta w$ or uw signals, P and N denote the terms conditionally averaged over the instances when $\Delta u \Delta w > 0$ and $\Delta u \Delta w < 0$ or $uw > 0$ and $uw < 0$. If $\overline{\Delta u \Delta w_{\mathrm{P}}}$ and $\overline{\Delta u \Delta w_{\mathrm{N}}}$ separately represent the scale wise contributions to counter-gradient and gradient fluxes, then one has to show that $\overline{\Delta u \Delta w_{\mathrm{P}}} \to 2\overline{uw_{\mathrm{P}}}$ and $\overline{\Delta u \Delta w_{\mathrm{N}}} \to 2\overline{uw_{\mathrm{N}}}$ as larger scales in the flow are accounted for.

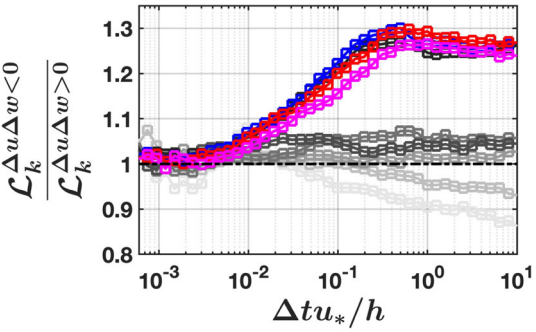

Fig. 10 For the GoAmazon dataset, the ratio $\mathscr{L}_k^{\Delta u\Delta w<0}/\mathscr{L}_k^{\Delta u\Delta w>0}$ are shown as line plots. The time-lags are normalized by the canopy time scale. The horizontal dash-dotted line indicates unity

Corresponding to RSL datasets, in Fig. 9, we plot the quantities $\overline{\Delta u\Delta w_{\mathrm{P}}}/2\overline{uw_{\mathrm{P}}}$ and $\overline{\Delta u\Delta w_{\mathrm{N}}}/2\overline{uw_{\mathrm{N}}}$ in panels (a) and (b), respectively. The time lags Δt are normalized by the canopy time scale. Although we present the results for RSL flows, conclusions remain the same even for ASL ones. The Figs. 9a, b clearly demonstrate that the quantities $\overline{\Delta u\Delta w_{\mathrm{P}}}$ and $\overline{\Delta u\Delta w_{\mathrm{N}}}$ indeed approach towards $2\overline{uw_{\mathrm{P}}}$ and $2\overline{uw_{\mathrm{N}}}$ as Δt increases significantly.

Therefore, at any Δt, $\overline{\Delta u\Delta w_{\mathrm{P}}}/2$ or $\overline{\Delta u\Delta w_{\mathrm{N}}}/2$ can be interpreted as how much the eddies cumulatively contribute to the counter-gradient or gradient fluxes at that scale. More importantly, the instantaneous values of $\Delta u\Delta w > 0$ ($\Delta u\Delta w < 0$) signals at any Δt carry the signatures of the counter-gradient (gradient) eddies pertaining to time scales smaller or equal to Δt. In accordance with Fig. 6, a strong height-dependence is observed for $\Delta u\Delta w > 0$ signals (Fig. 9a) as opposed to $\Delta u\Delta w < 0$ ones (Fig. 9b).

Ideally, the momentum flux structure functions should display a 4/3 scaling in the inertial subrange of the flow (Wyngaard 2010). However, when decomposed into positive and negative parts, it is apparent from Fig. 9 that the conditional structure functions $\overline{\Delta u\Delta w_{\mathrm{P}}}$ and $\overline{\Delta u\Delta w_{\mathrm{N}}}$ deviate from this expectation at smaller scales (see the cyan dash-dotted lines). This result awaits a theoretical explanation and addressing that is beyond the scope of the present study.

C Ratios of $\mathscr{L}_k$ Values

We demonstrate how the differences in the event-length statistics of gradient and counter-gradient momentum fluxes delineate between the eddy motions occurring at within and above the canopy air space. For that purpose, in Fig. 10, we plot the ratios of $\mathscr{L}_k$ values computed separately for the event lengths of $\Delta u\Delta w < 0$ and $\Delta u\Delta w > 0$ signals. One can clearly see, the ratio, $\mathscr{L}_k^{\Delta u\Delta w<0}/\mathscr{L}_k^{\Delta u\Delta w>0}$, remains closer or smaller than unity for heights within the canopy at all scales of the flow. However, for heights just above and beyond the canopy, these ratios exceed unity considerably. Therefore, this result indicates the importance of the counter-gradient eddies prevailing within the canopy air space.

Supplementary Information The online version contains supplementary material available at https://doi.org/10.1007/s10546-025-00908-x.

Acknowledgements SC and OP thank the support from the Research Council of Finland (Grant No. 354298). SC acknowledges the discussion with Jasper Vrugt, Efi Foufoula-Georgio, and Richard Vogel regarding the application of $\mathscr{L}$-moments in statistics. SC acknowledges Thara Prabhakaran and Anand Karipot for the use of CAIPEEX data for this research. For access to CAIPEEX dataset, one can contact thara@tropmet.res.in. SC thanks Keith McNaughton, Khaled Ghannam, Marcelo Chamecki, and Gaby Katul for the use of the SLTEST, GoAmazon, and Duke Forest datasets.

Funding Open access funding provided by Natural Resources Institute Finland.

Open Access This article is licensed under a Creative Commons Attribution 4.0 International License, which permits use, sharing, adaptation, distribution and reproduction in any medium or format, as long as you give appropriate credit to the original author(s) and the source, provide a link to the Creative Commons licence, and indicate if changes were made. The images or other third party material in this article are included in the article's Creative Commons licence, unless indicated otherwise in a credit line to the material. If material is not included in the article's Creative Commons licence and your intended use is not permitted by statutory regulation or exceeds the permitted use, you will need to obtain permission directly from the copyright holder. To view a copy of this licence, visit http://creativecommons.org/licenses/by/4.0/.

References

Bekker K (2024) lmom.m, MATLAB central file exchange. https://www.mathworks.com/matlabcentral/fileexchange/5874-lmom-m

Bonan G, Patton E, Harman I, Oleson K, Finnigan J, Lu Y, Burakowski E (2018) Modeling canopy-induced turbulence in the earth system: a unified parameterization of turbulent exchange within plant canopies and the roughness sublayer (CLM-ml v0). Geosci Model Dev 11(4):1467–1496

Brunet Y (2020) Turbulent flow in plant canopies: historical perspective and overview. Boundary-Layer Meteorol 177(2):315–364

Cava D, Katul G (2009) The effects of thermal stratification on clustering properties of canopy turbulence. Boundary-Layer Meteorol 130(3):307–325

Cava D, Katul G, Molini A, Elefante C (2012) The role of surface characteristics on intermittency and zero-crossing properties of atmospheric turbulence. J Geophys Res Atmos 117(D1)

Cava D, Dias-Júnior CQ, Acevedo O, Oliveira PE, Tsokankunku A, Sörgel M, Manzi AO, de Araújo AC, Brondani DV, Toro IMC et al (2022) Vertical propagation of submeso and coherent structure in a tall and dense Amazon forest in different stability conditions PART I: flow structure within and above the roughness sublayer. Agric For Meteorol 322(108):983

Chamecki M (2013) Persistence of velocity fluctuations in non-Gaussian turbulence within and above plant canopies. Phys Fluids 25(11):115110

Chamecki M, Dias NL, Salesky ST, Pan Y (2017) Scaling laws for the longitudinal structure function in the atmospheric surface layer. J Atmos Sci 74(4):1127–1147

Chowdhuri S (2024) L-moments reveal the scales of momentum transport in dense canopy flows. https://doi.org/10.5281/zenodo.14515878

Chowdhuri S, Banerjee T (2023) Revisiting "bursts" in wall-bounded turbulent flows. Phys Rev Fluids 8(4):044606

Chowdhuri S, Banerjee T (2024) Level crossings reveal organized coherent structures in a turbulent time series. Phys Rev Fluids 9(1):014601

Chowdhuri S, Prabha T (2019) An evaluation of the dissimilarity in heat and momentum transport through quadrant analysis for an unstable atmospheric surface layer flow. Environ Fluid Mech 19(2):513–542

Chowdhuri S, Kalmár-Nagy T, Banerjee T (2020) Persistence analysis of velocity and temperature fluctuations in convective surface layer turbulence. Phys Fluids 32(7):076601

Chowdhuri S, Ghannam K, Banerjee T (2022) A scale-wise analysis of intermittent momentum transport in dense canopy flows. J Fluid Mech 942:A51

Chung H, Koseff J (2021) Turbulence structure and scales in canopy-wake reattachment. Phys Rev Fluids 6(11):114605

Deshpande R, de Silva CM, Marusic I (2023) Evidence that superstructures comprise self-similar coherent motions in high Reynolds number boundary layers. J Fluid Mech 969:A10

Dias-Junior C, Marques FEP, Sa L (2015) A large eddy simulation model applied to analyze the turbulent flow above Amazon forest. J Wind Eng Ind Aerodyn 147:143–153

Dupont S, Patton EG (2022) On the influence of large-scale atmospheric motions on near-surface turbulence: comparison between flows over low-roughness and tall vegetation canopies. Boundary-Layer Meteorol 184(2):195–230

Everard K, Katul G, Lawrence G, Christen A, Parlange M (2021) Sweeping effects modify Taylor's frozen turbulence hypothesis for scalars in the roughness sublayer. Geophys Res Lett 48(22):e2021GL093746

Finnigan J (2000) Turbulence in plant canopies. Annu Rev Fluid Mech 32(1):519–571

Fuentes J, Chamecki M, dos Nascimento SRM, Von Randow C, Stoy P, Katul G, Fitzjarrald D, Manzi A, Gerken T, Trowbridge A et al (2016) Linking meteorology, turbulence, and air chemistry in the Amazon rain forest. Bull Am Meteorol Soc 97(12):2329–2342

Ghannam K, Poggi D, Porporato A, Katul G (2015) The spatio-temporal statistical structure and ergodic behaviour of scalar turbulence within a rod canopy. Boundary-Layer Meteorol 157(3):447–460

Ghannam K, Katul G, Bou-Zeid E, Gerken T, Chamecki M (2018) Scaling and similarity of the anisotropic coherent eddies in near-surface atmospheric turbulence. J Atmos Sci 75(3):943–964

Ghisalberti M, Nepf HM (2002) Mixing layers and coherent structures in vegetated aquatic flows. J Geophys Res Oceans 107(C2):1–3

Grinsted A, Moore JC, Jevrejeva S (2004) Application of the cross wavelet transform and wavelet coherence to geophysical time series. Nonlinear Process Geophys 11(5/6):561–566

Harman IN, Finnigan JJ (2007) A simple unified theory for flow in the canopy and roughness sublayer. Boundary-Layer Meteorol 123:339–363

Hosking J (2007) Some theory and practical uses of trimmed L-moments. J Stat Plan Inference 137(9):3024–3039

Hosking JR (1990) L-moments: analysis and estimation of distributions using linear combinations of order statistics. J R Stat 52(1):105–124

Katul G, Hsieh CI, Kuhn G, Ellsworth D, Nie D (1997) Turbulent eddy motion at the forest-atmosphere interface. J Geophys Res Atmos 102(D12):13409–13421

Launiainen S, Vesala T, Mölder M, Mammarella I, Smolander S, Rannik Ü, Kolari P, Hari P, Lindroth A, Katul G (2007) Vertical variability and effect of stability on turbulence characteristics down to the floor of a pine forest. Tellus B Chem Phys Meteorol 59(5):919–936

Li X, Hu L, Hu X, Liu W (2024) Scaling of vertical coherence and logarithmic energy profile for wall-attached eddies during sand and dust storms. J Fluid Mech 996:A7

Majumdar SN (1999) Persistence in nonequilibrium systems. Curr Sci 370–375

McNaughton K, Clement R, Moncrieff J (2007) Scaling properties of velocity and temperature spectra above the surface friction layer in a convective atmospheric boundary layer. Nonlin Process Geophys

Nair J, Wierman A, Zwart B (2022) The fundamentals of heavy tails: properties, emergence, and estimation, vol 53. Cambridge University Press, Cambridge

Nepf HM (2012) Flow and transport in regions with aquatic vegetation. Annu Rev Fluid Mech 44(1):123–142

Newman ME (2005) Power laws, pareto distributions and Zipf's law. Contemp Phys 46(5):323–351

Patton EG, Sullivan PP, Shaw RH, Finnigan JJ, Weil JC (2016) Atmospheric stability influences on coupled boundary layer and canopy turbulence. J Atmos Sci 73(4):1621–1647

Peltola O, Lapo K, Thomas C (2021) A physics-based universal indicator for vertical decoupling and mixing across canopies architectures and dynamic stabilities. Geophys Res Lett 48(5):e2020GL091615

Perret L, Patton EG (2021) Stability influences on interscale transport of turbulent kinetic energy and Reynolds shear stress in atmospheric boundary layers interacting with a tall vegetation canopy. J Fluid Mech 921:A14

Poggi D, Katul G (2009) Flume experiments on intermittency and zero-crossing properties of canopy turbulence. Phys Fluids 21(6):065103

Poggi D, Katul G (2010) Evaluation of the turbulent kinetic energy dissipation rate inside canopies by zero-and level-crossing density methods. Boundary-Layer Meteorol 136:219–233

Poggi D, Porporato A, Ridolfi L, Albertson J, Katul G (2004) The effect of vegetation density on canopy sub-layer turbulence. Boundary-Layer Meteorol 111:565–587

Raupach M, Thom A (1981) Turbulence in and above plant canopies. Annu Rev Fluid Mech 13(1):97–129

Raupach MR, Finnigan JJ, Brunet Y (1996) Coherent eddies and turbulence in vegetation canopies: the mixing-layer analogy. Boundary-Layer Meteorol 351–382

Sreenivasan K, Prabhu A, Narasimha R (1983) Zero-crossings in turbulent signals. J Fluid Mech 137:251–272

Thomas C, Foken T (2007) Flux contribution of coherent structures and its implications for the exchange of energy and matter in a tall spruce canopy. Boundary-Layer Meteorol 123(2):317–337

Thomson RE, Emery WJ (2014) Data analysis methods in physical oceanography. Newnes, Oxford

Torrence C, Compo GP (1998) A practical guide to wavelet analysis. Bull Am Meterol Soc 79(1):61–78

Vogel RM, Fennessey NM (1993) L moment diagrams should replace product moment diagrams. Water Resour Res 29(6):1745–1752

Wallace J (2016) Quadrant analysis in turbulence research: history and evolution. Annu Rev Fluid Mech 48:131–158

Wang Q (1996) Direct sample estimators of L moments. Water Resour Res 32(12):3617–3619

Wyngaard J (2010) Turbulence in the atmosphere. Cambridge University Press, Cambridge

Publisher's Note Springer Nature remains neutral with regard to jurisdictional claims in published maps and institutional affiliations.